Journal of Materials Chemistry A

ROYAL SOCIETY OF CHEMISTRY

PAPER

View Article Online
View Journal | View Issue

Cite this: J. Mater. Chem. A, 2026, 14, 8857

Investigation of the interface structure and electronic state of nanocomposite $La_{0.6}Sr_{0.4}Co_{0.2}Fe_{0.8}O_{3-\delta}$ and $Ce_{0.9}Gd_{0.1}O_{2-\delta}$ electrodes for solid oxide fuel cells

Daisuke Asakura, *[a] Tomohiro Ishiyama, *[a] Eiji Hosono, [a] Katherine Develos-Bagarinao, [b] Katsuhiko Yamaji, [a] Masaki Kobayashi, [cd] Miho Kitamura, [ef] Koji Horiba [ef] and Haruo Kishimoto [b]

Received 3rd July 2025
Accepted 6th January 2026

DOI: 10.1039/d5ta05378a

rsc.li/materials-a

The interface structure and electronic state of nanocomposite $La_{0.6}Sr_{0.4}Co_{0.2}Fe_{0.8}O_{3-\delta}$ (LSCF) and $Ce_{0.9}Gd_{0.1}O_{2-\delta}$ (gadolinium-doped ceria: GDC) electrodes for solid oxide fuel cells were investigated using scanning transmission electron microscopy (STEM) and soft X-ray absorption spectroscopy (XAS). The fine interface structure with compressive and extensive strains for LSCF and GDC, respectively, was observed by high-angle annular dark field STEM. The Fe $L_{2,3}$-edge total-electron-yield (TEY) XAS results showed a slight difference: the crystal field splitting for the FeO_6 octahedron of the LSCF and GDC nanocomposites is smaller than that of the LSCF bulk and thin film. This could be attributed to the strain effect at the interface. The Co $L_{2,3}$-edge TEY XAS results revealed that the valence of Co for the nanocomposite was 2+ with a high-spin (HS) configuration, while that for LSCF bulk was almost 3+ with a low-spin configuration. The Co^{2+} HS state, which should be less stable than the Co^{3+} LS state, is evidence that the oxygen adsorption/desorption reactivity is enhanced by the nanocomposite structure.

Introduction

Technologies that can convert energy from fuels such as hydrogen and methane to electricity are important to conserve the amount of energy used to achieve carbon neutrality. Among them, solid oxide fuel cells (SOFCs) are a promising technology for electrical power generation systems. The efficiency of energy conversion from fuel to electricity of SOFCs is higher compared to the efficiency of other fuel cell systems such as polymer electrolyte membrane-type fuel cells.[1,2] In order to enhance the further spread of SOFCs, it is necessary to improve their efficiency and reduce costs. Improving the electrical generation performance of SOFCs by increasing the current density and reducing the overpotential for the oxygen electrode is one of the most direct approaches. It is well known that the dominant step of the cathode reaction is the adsorption of molecular oxygen and its dissociation into oxygen atoms at the electrode surface. Because this electrochemical reaction mainly occurs at the triple phase boundary (TPB) formed by the electrode, electrolyte, and gas phases, increasing the TPB length and improving the activity at the TPB can reduce the electrode resistance. Mixed conducting materials with oxide ions and holes, such as $La_{0.6}Sr_{0.4}Co_{0.2}Fe_{0.8}O_{3-\delta}$ (LSCF), can cause the reaction to occur at the double phase boundary (DPB) of the electrode surface and gas interface, and this contributes to enlarging the active region for cathode reactions. In both cases using the TPB and DPB, the enhancement of activity at the electrode surface is the most important parameter to reduce the electrode resistance.

To enlarge the TPB length, Develos-Bagarinao *et al.* have fabricated a composite electrode of LSCF and $Ce_{0.9}Gd_{0.1}O_{2-\delta}$ (gadolinium-doped ceria: GDC) controlled in nanometer scale, as shown in Fig. 1.[3] The LSCF and GDC nanocomposite (referred to as LSCF/GDC nanocomposite) electrode can enlarge the TPB length drastically, and it is confirmed that it effectively works to reduce the electrode resistance using a cathode for fuel cell operation. Compared to conventional porous LSCF electrode layers alone, the electrodes developed in this study demonstrated significantly enhanced power generation performance, exhibiting current densities of approximately 2.2 A cm^{-2} at 650 °C and 4.7 A cm^{-2} at 700 °C under an operating voltage of

[a]Research Institute for Energy Efficient Technologies, National Institute of Advanced Industrial Science and Technology (AIST), 1-1-1 Higashi, Tsukuba, Ibaraki 305-8565, Japan. E-mail: daisuke-asakura@aist.go.jp; tomohiro.ishiyama@aist.go.jp
[b]Global Zero Emission Research Center, National Institute of Advanced Industrial Science and Technology (AIST), 16-1 Onogawa, Tsukuba, Ibaraki 305-8569, Japan
[c]Center for Spintronics Research Network, The University of Tokyo, 7-3-1 Hongoa, Bunkyo-ku, Tokyo 113-8656, Japan
[d]Department of Electrical Engineering and Information Systems, The University of Tokyo, 7-3-1 Hongo, Bunkyo-ku, Tokyo 113-8656, Japan
[e]NanoTerasu Center, National Institutes for Quantum Science and Technology (QST), 6-6-11-901 Aoba, Aramaki, Aoba-ku, Sendai, Miyagi 980-8579, Japan
[f]Photon Factory, Institute of Materials Structure Science, High Energy Accelerator Research Organization (KEK), 1-1 Oho, Tsukuba, Ibaraki 305-0801, Japan

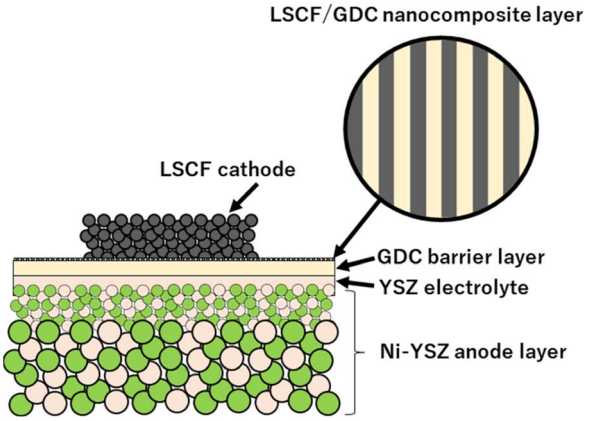

Fig. 1 Schematic of the SOFC cell with the LSCF/GDC nanocomposite layer.

0.7 V. These results indicate that the nanoengineering approach is highly effective in dramatically improving electrode performance. Furthermore, the fabricated electrode layers were found to consist of laterally ordered periodic nanostructures with alternating several-nanometer regions of LSCF and GDC, forming highly coherent lattice-matched interfaces. This result suggests that the formation of such hetero-interfaces, rather than simply introducing nanoscale interfaces, may induce lattice distortions that affect electrode properties. Modulation of material properties by lattice distortion has been reported in several notable cases. For example, the $SrTiO_3$/YSZ interface has been shown to exhibit ultrafast oxygen ionic conductivity.[4] Furthermore, a remarkable enhancement of the oxygen surface exchange rate has been observed at the interface between the $La_{1-x}Sr_xCoO_3$ (LSC113) and $La_{2-x}Sr_xCoO_4$ (LSC214) phases.[5,6] In the context of oxygen adsorption/desorption reactions, a correlation has been reported between the electronic structure of the electrode surface and reactivity, *i.e.*, the surface exchange coefficient.[7] It has been reported that strain generated as a result of thin-film formation at heterointerfaces can induce changes in the electronic structure that affect oxygen adsorption and desorption reactions.[8] This suggests the potential of nanoscale-controlled heterointerfaces to enhance surface activity.

To elucidate the origin of the high activity observed in previously reported LSCF/GDC nanocomposite electrode layers fabricated *via* pulsed laser deposition (PLD), a detailed analysis of the introduced lattice strain and corresponding electronic structure was conducted. The lattice strain was analyzed in terms of both direction and magnitude using geometric phase analysis (GPA)[9] applied to scanning transmission electron microscopy (STEM) high-angle annular dark field (HAADF) images. The electronic state of the LSCF/GDC nanocomposite is discussed based on the results of soft X-ray absorption spectroscopy (XAS). The valence states of Fe and Co and information on the Fe–O/Co–O bonds are investigated. Also, XAS measurements of single-phase LSCF and GDC were performed for comparison.

To achieve further performance improvements in electrochemical devices such as SOFCs and solid oxide electrolysis cells (SOECs), it is essential to utilize technologies that enable more precise control of microstructures than ever before. This involves not only enhancing the functionality of bulk materials but also actively leveraging nanoscale structural control and enhancement of unique properties arising from strain effects, as discussed in this paper.

In this study, the electronic states of cobalt and iron in an LSCF-GDC nanocomposite electrode deposited on a polycrystalline substrate are clarified through advanced soft X-ray spectroscopic electronic structure analysis with spectrum calculations. The observed changes in the electronic structure induced by strain effects provide new insights into the modification of material properties, offering a novel understanding that can contribute to advancements in the research field of SOFCs.

Method

LSCF raw powder was purchased from Noritake (Japan). The LSCF pellet was prepared as a bulk sample by pressing raw powder using uniaxial and cold-isostatic-pressing apparatuses with pressures of 10 MPa and 390 MPa, respectively, and sintering at 1300 °C for 5 hours. The GDC raw powder was purchased from Shin-Etsu Chemical (Japan). The GDC pellet was also prepared as a bulk sample by pressing raw powder in the same way as LSCF and sintering at 1400 °C for 5 hours. The LSCF and GDC pellets were also used as target materials in a PLD process. The LSCF/GDC nanocomposite layer was fabricated on GDC pellets by the PLD method using a KrF excimer laser at a wavelength of 315 nm as previously reported.[3] To control the crystallinity, the substrate temperature during deposition was kept at 650 or 750 °C. Single-phase layers of LSCF and GDC were also fabricated on GDC pellets to investigate whether the change in electronic structure was due to the PLD process or to the formation of the hetero interphase in the nanocomposite structure.

The STEM-HAADF images were obtained using a Tecnai Osiris TEM (FEI) with an acceleration voltage of 200 kV. The specimen for STEM analysis was prepared by focused ion beam (FIB) microscopy. The lattice image obtained from STEM-HAADF measurements was analyzed to calculate the difference of lattice plane distances between the LSCF and GDC phases by the GPA method[9] with the plugin in the Digital Micrograph (GMS3.0) environment.

XAS measurements were performed at the BL-2B of the Photon Factory, KEK (Tsukuba, Japan). Surface-sensitive total electron yield (TEY) and bulk-sensitive partial fluorescence yield (PFY) modes were employed. A silicon drift detector (SDD; XR100-FastSDD made by Amptek) was used for the PFY detection. The incident X-rays were normal to the sample surface, and the SDD detected the photons emitted to the 45° direction. The polarization dependence of the incoming X-rays in the *x*-*y* plane of the sample could be considered negligible because there are many small domains randomly rotated within the beam size (approximately 100 μm (V) × 500 μm (H)). All the measurements were conducted under a high vacuum environment of $<1 \times 10^{-5}$ Pa at room temperature.

The Co/Fe $L_{2,3}$-edge (2p-3d absorption) TEY XAS spectra were analyzed with a CTM4XAS program that is a charge-transfer multiplet (CTM) calculation.[10] The calculation is based on ligand-field theory: a MO_6 octahedron (M = Fe, Co) with the M 3d and 2p and O 2p orbitals in O_h symmetry is considered a model cluster. The charge-transfer (CT) effect from the O 2p to the M 3d orbitals is treated as a configuration interaction with electron configurations like d^n, $d^{n+1}L^1$, and $d^{n+2}L^2$ (L denotes a ligand hole created by the CT).

Results and discussion

STEM-HAADF analysis

Fig. 2a shows the STEM-HAADF image of the LSCF/GDC nanocomposite. Phase contrasts are clearly observed, and these contrasts indicate that the dark areas are LSCF phases and the white areas are GDC phases, as reported in previous STEM-EDS analysis.[3] In Fig. 2b and c, the lattice difference analyzed by the GPA method is shown for the *x* and *y* directions, respectively. The colormap indicates the degree of the differences against the average value of the lattice plane distances in the *x* and *y* directions of the LSCF and GDC phases determined from the spot in the diffraction images. For the GPA analysis result in the *x* direction, the colormap is shown with red and blue and these colors indicate that the lattice plane distance is larger and smaller than the reference value, respectively. This is consistent with the difference in lattice size between the original LSCF and GDC phases. These correspond to the (012) (ap. 3.90 Å) and (010) (ap. 2.70 Å) planes of LSCF and GDC, as shown in Fig. 3a and b. In contrast, the GPA analysis results in the *y* direction show the colormap to be almost green, indicating that the lattice mismatch is smaller in this direction.

As shown in Fig. 3a and b, the lattice plane distances corresponding to the *y* direction of the STEM images are 2.76 Å for LSCF and 2.70 Å for GDC; although the lattice size of LSCF is originally larger than that of GDC, the lattices are aligned at this heterogeneous interface. According to the interfacial structure consisting of the [110] of LSCF and [200] of GDC, as shown in Fig. 3, the lattice mismatch is calculated to be 2.1% (=0.2765/0.2709). Thus, the LSCF lattice is compressed and the GDC lattice expanded along the direction at the interface. Both LSCF and GDC have intrinsic oxygen vacancies, and it is possible that the interface shown in Fig. 3c may also contain oxygen vacancies. However, it should be noted that this is a minor structural arrangement. For clarity and convenience, the interface layer is depicted in Fig. 3c as being completely occupied by oxygen. The

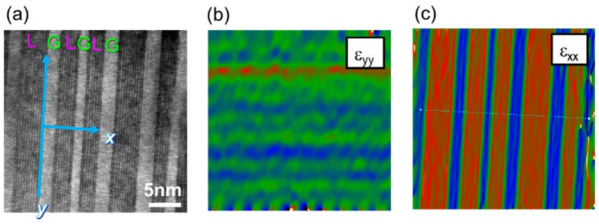

Fig. 2 (a) STEM-HAADF image of the LSCF/GDC nanocomposite. GPA analysis mapping along (b) *y* direction and (c) *x* direction.

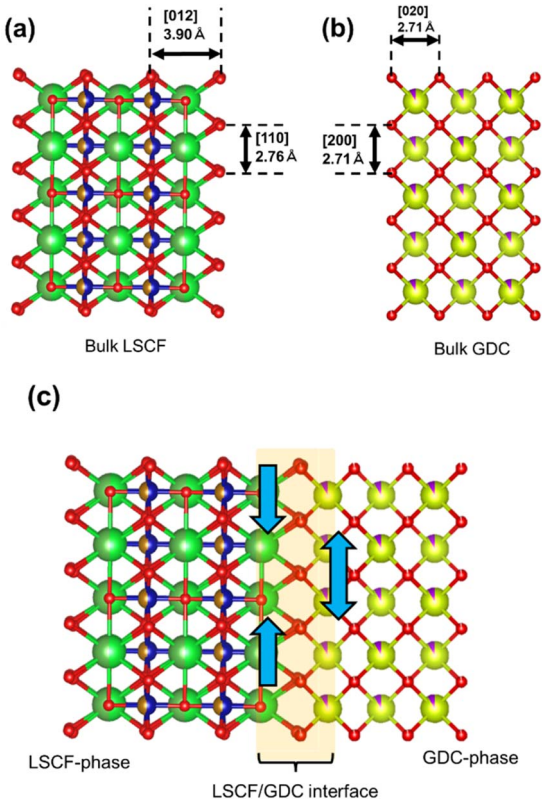

Fig. 3 Structure of (a) LSCF and (b) GDC analysed from the STEM-HAADF results. (c) An image of the lattice strain in LSCF and GDC interface. (The figure was visualized using VESTA software.[16]).

number of oxygen atoms is consistent at the interface between LSCF and GDC, as shown in Fig. 3c. To aid understanding, projections of the interface oxygen atoms for LSCF and GDC are provided in SI (Fig. S1 and S2). The strain should contribute to enhance the oxygen exchange reaction at the surface of the nanocomposite electrode, as Lee *et al.* reported.[8] In their report, DFT calculations indicated that the O 2p band center is elevated toward the Fermi level by the lattice expansion.

The thermal expansion coefficients of LSCF and GDC are 15.3×10^{-6} K^{-1} and 13.5×10^{-6} K^{-1}, respectively,[11] indicating that LSCF exhibits larger thermal expansion. Therefore, under high-temperature operating conditions, the lattice mismatch between the two materials is expected to increase, making the effects of strain even more significant.

Fe $L_{2,3}$-edge XAS

Fig. 4 shows the Fe $L_{2,3}$-edge TEY XAS spectra. The spectra for the LSCF bulk and the as-deposited film are almost the same. The line shape is similar to those of $LaFeO_3$ (ref. 12) and typical trivalent iron oxides such as Fe_2O_3.[13,14] Indeed, the CTM calculation for a Fe^{3+} HS state with an O_h symmetry well reproduces the experimental spectra (Fig. 5). The values of the crystal-field splitting 10*Dq*, CT energy from the O 2p to Fe 3d orbitals Δ, d-electron Coulomb interaction *U*, and core-hole potential *Q* are 1.1, 2.0, 5.0, and 6.0 eV, respectively (case (i) in Table 1). Similar values of Δ for $LaFeO_3$ series have been reported.[15]

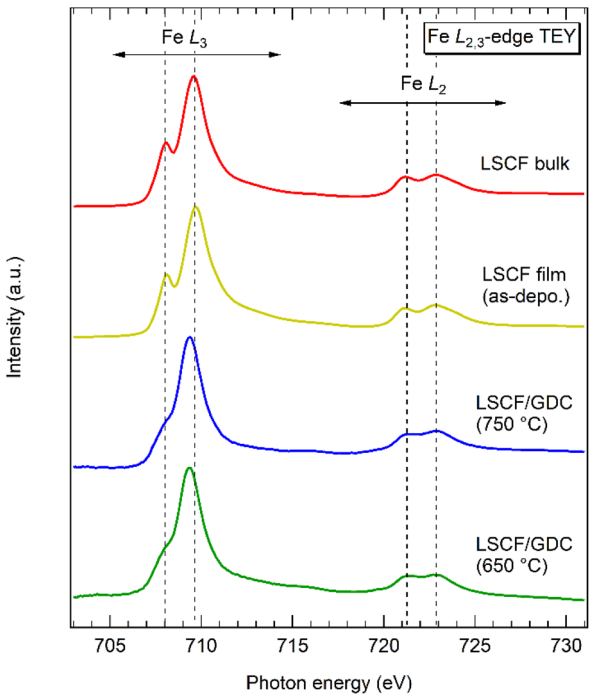

Fig. 4 Fe $L_{2,3}$-edge TEY XAS spectra for the LSCF bulk, as-deposited film, and nanocomposites.

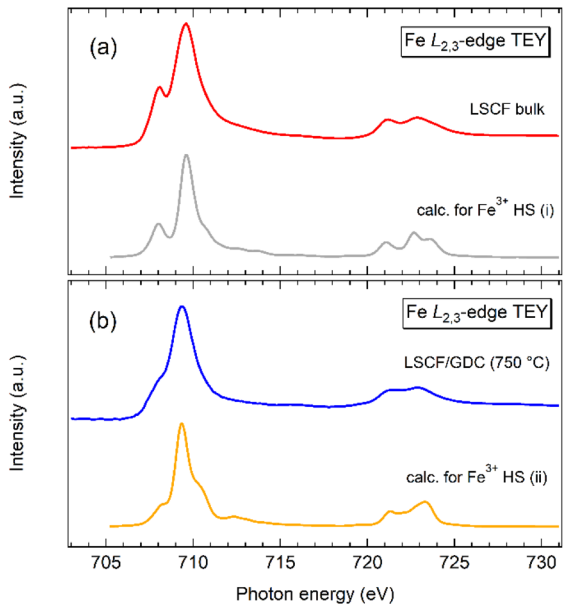

Fig. 5 Comparisons between the Fe $L_{2,3}$-edge experimental TEY XAS spectra and CTM calculations. (a) LSCF bulk and calculation for a Fe^{3+} HS state. (b) Nanocomposite (750 °C) and calculation for another Fe^{3+} HS state. The electronic-structure parameters used in the calculations are summarized in Table 1.

For the nanocomposite samples, the highest L_3 peak is slightly shifted to the lower energy side, and the dip between that peak and the 708.0 eV peak becomes ambiguous compared to the spectra of the LSCF bulk and the as-deposited film. Also,

Table 1 Electronic structure parameters (selected) used in the CTM calculation for the Fe $L_{2,3}$-edge TEY XAS spectra (in eV)

	Fe^{3+} HS(i)	Fe^{3+} HS(ii)
$10Dq$	1.1	0.5
U	5.0	5.0
Q	6.0	6.0
Δ	2.0	3.0

slight changes are observed for the L_2-edge of the nanocomposite samples. The CTM calculation for a Fe^{3+} HS state with $10Dq = 0.5$ eV, $\Delta = 3.0$ eV, $U = 5.0$ eV, and $Q = 6.0$ eV (case (ii) in Table 1) reproduced the spectra of the nanocomposite samples (Fig. 5). The $10Dq$ of 0.5 eV is a very small value that is necessary to reproduce the gradual shoulder structure around 708.0 eV.

The small $10Dq$ indicates a very weak crystal field; the Fe–O bond should be elongated compared to that in bulk LSCF. STEM-HAADF analysis revealed that the M–O bonds are compressed along the interface. However, according to the Poisson effect, the M–O bonds perpendicular to the interface are expected to be elongated. Most likely, the present XAS and CTM calculation, where O_h symmetry is considered, strongly reflect the vertical direction to the interface, while the XAS measurement with a large incident beam detects the average information of the randomly oriented nanocomposite domains. The small $10Dq$ also suggests that the interaction between the Fe 3d and O 2p orbitals should be weakened in the nanocomposites. In addition, Δ is larger than that for (i), corresponding to the CT effect and hybridization being a little weaker in the nanocomposites.

Another possibility for the difference in the Fe $L_{2,3}$-edge line shape between the LSCF (bulk and film) and LSCF/GDC nanocomposites could be the valence change of Fe. The gradual shoulder structure around 708.0 eV in the Fe L_3-edge TEY XAS for the nanocomposites is similar to that for $La_{0.5}Sr_{0.5}FeO_3$ (ref. 12) and $Sr_2FeCoO_{6-\delta}$ (ref. 17) where the Fe^{4+} and Fe^{3+} states coexist. In addition, a similar line shape was reported for ion-implanted $LaFeO_3$ thin film,[18] where a change in the average Fe valence has been suggested. However, the highest Fe L_3-edge peak position of the nanocomposites is slightly lower than that of the LSCF bulk with the Fe^{3+} state. Moreover, the width of the Fe L_3-edge XAS for the nanocomposites is narrower than those for $SrFeO_3$,[12] $BaFeO_3$ (ref. 19) and $CaFeO_3$,[20,21] which have only the Fe^{4+} state. The doublet peaks of Fe L_2-edge (around 721.2 and 722.9 eV) in Fig. 5b have a similar height, which is contrary to the peak around 722.9 eV that is clearly higher for the Fe^{4+} materials.[19,22] Thus, the Fe $L_{2,3}$-edge line shape of the nanocomposites does not suggest oxidation to the Fe^{4+} state. Indeed, the CTM calculations for some Fe^{4+} states did not reproduce the experimental results of the nanocomposites at all (Fig. S3 in SI). The difference in the Fe $L_{2,3}$-edge line shape is solely explained by the difference in $10Dq$ and Δ in the Fe^{3+} electron configuration.

While the saturation/self-absorption effects deform the line shape for the PFY spectra to some extent,[23–27] the Fe $L_{2,3}$-edge

PFY XAS spectra of the nanocomposites showed similar profiles to the TEY results: the peak at 708.0 eV decreased and the L_3 main peak slightly shifted to the lower energy side in the nanocomposites (Fig. S4 in SI). Therefore, the weakened interaction on the Fe 3d-O 2p hybridization on average should be uniform from the surface to the bulk region at least as deep as ~1 μm from the surface.

On the other hand, the Fe $L_{2,3}$-edge PFY XAS spectra of the LSCF bulk and as-deposited film are different to some extent from their Fe $L_{2,3}$-edge TEY XAS spectra (Fig. S2 in SI). The PFY line shapes are partly similar to those for $CaFeO_3$.[20,21] Thus, the LSCF bulk and as-deposited film should include some Fe^{4+} components in addition to the Fe^{3+} components in their bulk region.

Co $L_{2,3}$-edge XAS

The Co $L_{2,3}$-edge TEY XAS spectra for the LSCF bulk, as-deposited LSCF film, and nanocomposites are shown in Fig. 6. For the LSCF bulk, the highest peaks at the L_3 and L_2 edges are located at 779.4 and 793.7 eV, respectively, which is similar to the spectra of some trivalent Co oxides including $LaCoO_3$ families.[28–31] Indeed, the CTM calculation for a Co^{3+} low-spin (LS) state reproduces the main peaks at 779.4 and 793.7 eV (Fig. 7a). The electronic structure parameters used in the Co^{3+} LS calculation are summarized in Table 2. The determined crystal field splitting $10Dq$ is 1.5 eV which is high enough to realize the LS state. The CT energy from the O 2p to Co 3d orbitals, Δ, was determined to be 1.0 eV, suggesting a strong CT effect. On the other hand, the shoulder structure around 777.8 eV for the experimental spectrum of the LSCF bulk is higher than the corresponding structure in the calculated spectrum for the Co^{3+} LS state. This shoulder structure is attributed to a small amount of coexisting Co^{2+}, as discussed later.

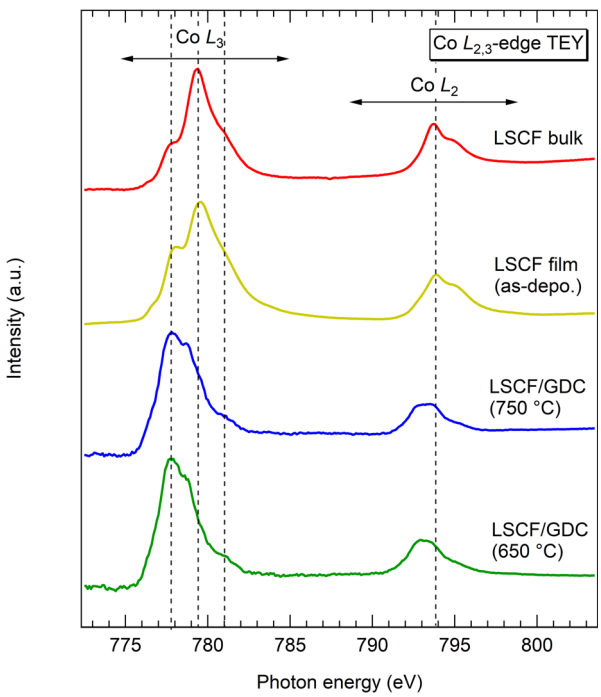

Fig. 6 Co $L_{2,3}$-edge TEY XAS spectra for the LSCF bulk, as-deposited LSCF film, and LSCF/GDC nanocomposites.

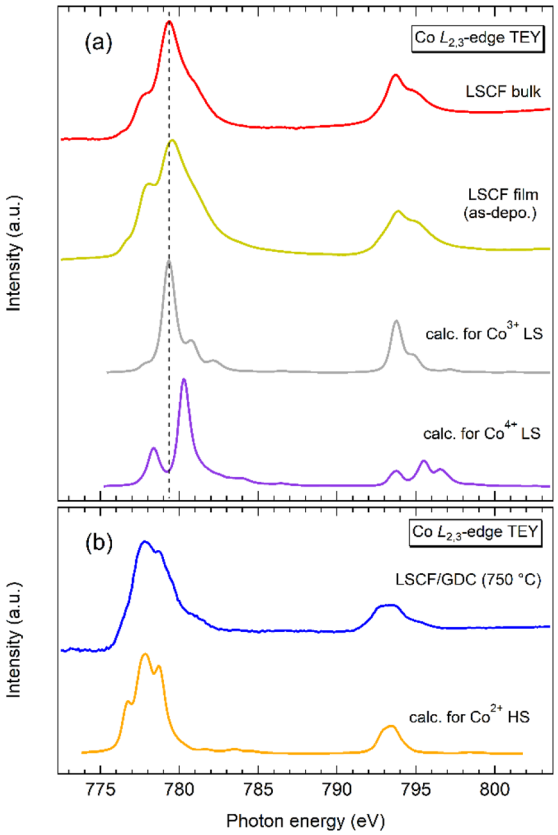

Fig. 7 Comparisons between the Co $L_{2,3}$-edge experimental TEY XAS spectra and CTM calculations. (a) LSCF bulk, LSCF film and calculations for a Co^{3+} LS state and a Co^{4+} LS state. (b) Nanocomposite (750 °C) and calculation for a Co^{2+} HS state. The electronic-structure parameters used in the calculations are summarized in Table 2.

For the spectrum of the as-deposited LSCF film, the structures around 777.8 and 792.8 eV increase, suggesting that more Co^{2+} sites are involved. In addition, the shoulder structure around 781.0 eV increases and the main peaks of the L_3 and L_2 edges slightly shift by ~0.2 eV to the higher energy side compared to the LSCF bulk (see Fig. S5 in the SI). This change suggests that a Co^{4+} LS state also exists, because the main peaks of the Co^{4+} state shift to the higher energy side, as the Co^{4+} calculation indicates in Fig. 7a. A similar change with an increase of the Co^{4+} state has been reported for the Co $L_{2,3}$-edge XAS of $Li_{1-x}CoO_2$.[32–34]

Table 2 Electronic structure parameters (selected) used in the CTM calculation for the Co $L_{2,3}$-edge TEY XAS spectra (in eV)

	Co^{3+} LS	Co^{4+} LS	Co^{2+} HS
$10Dq$	1.5	1.5	0.5
U	5.0	5.0	5.0
Q	6.0	6.0	6.0
Δ	1.0	1.0	2.0

The spectra for the nanocomposites fabricated at 650 and 750 °C are almost the same, while the line shapes are greatly different from those for the LSCF bulk and the as-deposited film (Fig. 6). They are similar to the spectra of some divalent Co oxides such as CoO.[35,36] As Fig. 7b shows, the spectrum for the nanocomposite (750 °C) is mostly reproduced by the CTM calculation for a Co^{2+} high-spin (HS) state. The dominant Co^{2+} HS state is characteristic of the nanocomposite samples. The determined value of 10*Dq* of 0.5 eV, which is small enough to maintain the HS state with the d^7 configuration, is obviously smaller than the 10*Dq* of 1.5 eV for the Co^{3+} LS state found in the LSCF bulk and the as-deposited film. The weaker 10*Dq* for the Co^{2+} HS state of the nanocomposites suggests that the Co–O bond is elongated, which is compatible with the formal ionic radius of the Co^{2+} HS state (0.745 Å) being larger than that of the Co^{3+} LS state (0.545 Å).[37] Therefore, the Co 3d-O 2p hybridization on the Co–O bond near the surface and interface to GDC should be modified together with the reduction by the nanocomposite structure.[28,38] This modification is analogous to the Fe $L_{2,3}$-edge results, while the analysis by STEM indicates that the LSCF and GDC at the interface are compressed and expanded, respectively.

For the bulk-sensitive Co $L_{2,3}$-edge PFY spectra, a similar trend to the TEY results was observed, while the Co^{2+} HS state is enhanced for the nanocomposite of 650 °C compared to that of 750 °C (Fig. S6 in SI). Thus, the reduction of Co is confirmed up to ~1 μm from the surface.

O K-edge TEY XAS

O K-edge (1s-2p absorption) XAS is useful to simply discuss the unoccupied states, considering hybridization of the O 2p orbital and orbitals of the neighboring elements.[39] Fig. 8a is the O K-edge TEY XAS results for the LSCF (bulk and film), LSCF/GDC nanocomposites, and GDC (bulk and film). For the LSCF bulk and film, pre-edge peaks below 532.5 eV correspond to the O 2p-Co 3d/Fe 3d hybridization, and peaks at 533.0–538.5 eV are of the O 2p-Sr 4d/La 5d hybridization.[12,28,38] The peaks centered at 528.3 and 531.5 eV for the LSCF film are enhanced compared to those for the LSCF bulk. These changes originate from the different Co 3d states between the film and bulk, because the Fe $L_{2,3}$-edge XAS line shape is almost the same (Fig. 4). The peak enhancements should correspond to the existence of the small amount of Co^{4+} state in the LSCF film, as discussed for the Co $L_{2,3}$-edge results (Fig. 7a).

In contrast to the LSCF film and bulk, the O K-edge TEY XAS spectra for the LSCF/GDC nanocomposites strongly reflect the line shape of GDC. The peaks centered at 530.3, 532.8, and 537.5 eV for the GDC bulk and film are respectively attributed to the orbitals hybridized with Ce 4f, 5d (e_g), and 5d (t_{2g}),[40–44] while contribution by Gd should have broad structures in the whole region.[45] Note that the Ce 4f state was almost the same among the samples (see the Ce $M_{4,5}$-edge XAS results shown in Fig. S7 in SI).

To compare the unoccupied Co and Fe 3d orbitals between the LSCF bulk/film and nanocomposites suppressing the contribution from GDC in the nanocomposites, we made a difference spectrum: [LSCF/GDC (750 °C)] – 0.3 × [GDC bulk]

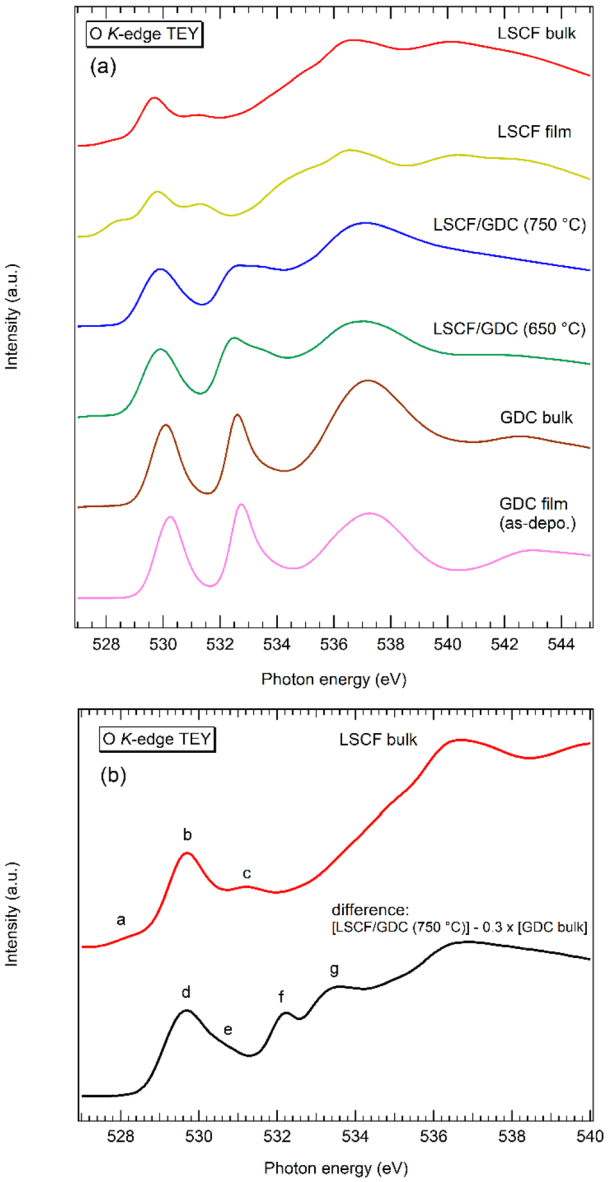

Fig. 8 (a) O K-edge TEY XAS spectra for the LSCF bulk, LSCF film, LSCF/GDC nanocomposites, GDC bulk, and GDC film. (b) Comparison of the spectrum of the LSCF bulk and a difference spectrum given by [LSCF/GDC (750 °C)] – 0.3 × [GDC bulk].

(Fig. 8b). Compared to the spectrum for the LSCF bulk, the difference spectrum does not have peaks around 528.2 eV. The disappearance of peak a of the LSCF bulk indicates that the valence of Co is lower (reduced) than the LSCF bulk. On the other hand, two peaks exist at 532.2 (peak f) and 533.6 eV (peak g) in the difference spectrum. These peaks indicate an increase of the Co^{2+} state because the O K-edge XAS of CoO has similar peaks.[35] These considerations are consistent with the Co $L_{2,3}$-edge results.

Discussion

As the Co $L_{2,3}$-edge XAS results show, the Co sites for the nanocomposites are reduced to the Co^{2+} state. The Co^{2+} HS

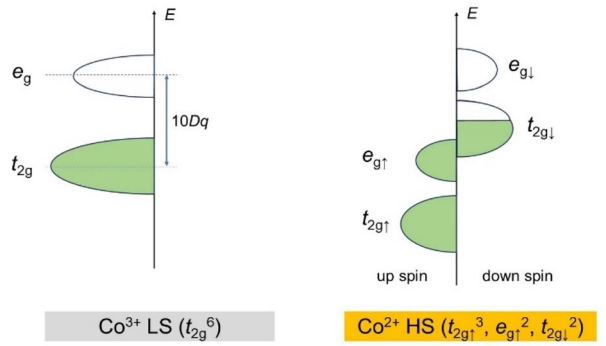

Fig. 9 Schematic of 3d orbitals of the Co^{3+} (d^6) LS and Co^{2+} (d^7) HS states. The $t_{2g\downarrow}$ orbital for the Co^{2+} HS state is not fully occupied.

state ($t_{2g\uparrow}^3$, $e_{g\uparrow}^2$, $t_{2g\downarrow}^2$) observed for the nanocomposites should be more reactive to the oxygen adsorption/desorption reaction than the Co^{3+} LS state (t_{2g}^6) with a closed shell for the t_{2g} orbital (Fig. 9). The partially occupied $t_{2g\downarrow}$ orbital for the Co^{2+} HS state can easily contribute to such reactions.[46]

As discussed above, the Fe $L_{2,3}$-edge TEY XAS results of the nanocomposites suggest the following possibilities. The weakened Fe 3d-O 2p hybridization with the elongation of the Fe–O bond perpendicular to the LSCF/GDC interface is consistent with the results of the STEM-HAADF, at least for that direction. The weakened interaction possibly contributes to enhance the mobility of oxide ions. The stabilization of cobalt in a lower valence state may also contribute to an increase in oxygen vacancy concentration in the perovskite structure, which may help improve oxide ion conductivity.

Assuming that all Co ions are in the divalent state and all Fe ions are in the trivalent state, charge neutrality is achieved for the composition $La_{0.6}Sr_{0.4}Co_{0.2}Fe_{0.8}O_{2.7}$, corresponding to an oxygen vacancy concentration of $\delta = 0.3$. Such high oxygen vacancy concentrations ($\delta = 0.3$) typically destabilize the crystal structure in conventional bulk materials, as they can induce reduction decomposition. However, in this study, the formation of heterointerfaces may contribute to the stabilization of the perovskite structure, thereby maintaining a highly active state with a high concentration of oxygen vacancies.

Changes in the electronic structure induced the lattice strain at such heterointerfaces have previously been observed in the in-plane direction at interfaces between thin films and substrates. However, the present study confirms that the formation of these interfaces in the out-of-plane direction allows direct contact with the gas phase and functions effectively as an active site for electrode reactions. Furthermore, nanostructuring has created numerous hetero-interfaces, effectively utilizing strain-induced highly active surfaces as reaction sites. The LSCF/GDC nanocomposite electrode layer fabricated by PLD effectively promoted oxygen adsorption and desorption reactions at the surface due to the presence of Co^{2+}. Despite its dense structure, ion diffusion resistance was not a limiting factor. This may be attributed to the weakening of the Fe–O crystal field and the increased concentration of oxygen vacancies, both of which are assumed to have promoted fast oxygen ion diffusion at the LSCF/GDC interface.

Conclusions

The LSCF/GDC nanocomposite with the enhanced power generation performance has interfacial strains on both the LSCF and GDC sides, as the STEM-HAADF measurements and GPA analysis revealed. The LSCF layer was found to be compressed along the interface while the GDC layer was extended. For the perpendicular direction to the interface, the extension of the LSCF layer was expected. Simultaneously, the electronic structure of the LSCF layer is modified by the strains compared to those of LSCF bulk and the thin film without the heterostructure.

The Fe $L_{2,3}$-edge TEY XAS line shape for the nanocomposites showed slight changes, suggesting a decrease in the interaction of the Fe 3d-O 2p orbitals on average for all directions. This should enhance the oxide ion conductivity. The Co $L_{2,3}$-edge TEY XAS spectra for the nanocomposites were clearly attributed to the Co^{2+} HS state, while that for the LSCF bulk suggested that the Co^{3+} LS state was dominant. The electronic structure change in Co by the nanocomposite structure could increase the oxygen release/adsorption reactivity because the Co^{2+} HS state is less stable than the Co^{3+} LS state. The O K-edge XAS results support the enhanced Co^{2+} HS state in the nanocomposites. These electronic-structure analyses by XAS will contribute to developing novel electrode materials/structure for SOFCs with high performances.

Author contributions

Daisuke Asakura: supervision, investigation, writing – original draft. Tomohiro Ishiyama: supervision, investigation, writing – original draft. Eiji Hosono: investigation. Katherine Develos-Bagarinao: supervision, investigation, writing – review & editing. Katsuhiko Yamaji: supervision, writing – review & editing. Masaki Kobayashi: investigation. Miho Kitamura: investigation. Koji Horiba: investigation. Haruo Kishimoto: supervision, writing – review & editing.

Conflicts of interest

There are no conflicts to declare.

Data availability

The data supporting this article have been included as part of the supplementary information (SI). Supplementary information is available. See DOI: https://doi.org/10.1039/d5ta05378a.

Acknowledgements

The XAS measurements were conducted at the Photon Factory with the approval of the Photon Factory Advisory Committee (Proposal No. 2020G118 and 2022G094). This work was partly supported by JSPS KAKENHI Grant Number 22K05059 and the Spintronics Research Network of Japan (Spin-RNJ).

References

1 Ro. Peters, W. Tiedemann, I. Hoven, R. Deja, N. Kruse, Q. Fang, D. Schäfer, F. Kunz, L. Blum, R. Peters and R.-A. Eichel, *J. Electrochem. Soc.*, 2023, **170**, 044509.

2 K. Nakamura, T. Ide, S. Taku, T. Nakajima, M. Shirai, T. Dohkoh, T. Kume, Y. Ikeda, T. Somekawa, T. Kushi, K. Ogasawara and K. Fujita, *Fuel Cells*, 2017, **17**, 535–540.

3 K. Develos-Bagarinao, T. Ishiyama, H. Kishimoto, H. Shimada and K. Yamaji, *Nat. Commun.*, 2021, **12**, 3979.

4 J. Garcia-Barriocanal, A. Rivera-Calzada, M. Varela, Z. Sefrioui, E. Iborra, C. Leon, S. J. Pennycook and J. Santamaria, *Science*, 2008, **321**, 676–680.

5 M. SASE, *Solid State Ionics*, 2008, **178**, 1843–1852.

6 M. Sase, F. Hermes, K. Yashiro, K. Sato, J. Mizusaki, T. Kawada, N. Sakai and H. Yokokawa, *J. Electrochem. Soc.*, 2008, **155**, B793.

7 R. Jacobs, T. Mayeshiba, J. Booske and D. Morgan, *Adv. Energy Mater.*, 2018, **8**, 1702708.

8 D. Lee, R. Jacobs, Y. Jee, A. Seo, C. Sohn, A. V. Ievlev, O. S. Ovchinnikova, K. Huang, D. Morgan and H. N. Lee, *J. Phys. Chem. C*, 2017, **121**, 25651–25658.

9 M. J. Hÿtch, E. Snoeck and R. Kilaas, *Ultramicroscopy*, 1998, **74**, 131–146.

10 E. Stavitski and F. M. F. de Groot, *Micron*, 2010, **41**, 687–694.

11 A. A. Solovyev, I. V. Ionov, A. V. Shipilova and P. D. Maloney, *J. Electroceram.*, 2018, **40**, 150–155.

12 M. Abbate, F. M. F. De Groot, J. C. Fuggle, E. D. Nij, N. A. Fujimori, O. Strebel, F. Lopez, M. Domke, G. Kaindl, G. A. Sawatzky, M. Takano, Y. Takeda, H. Eisaki and S. Uchida, *Phys. Rev. B: Condens. Matter Mater. Phys.*, 1991, **46**, 4511–4519.

13 J. Miyawaki, S. Suga, H. Fujiwara, M. Urasaki, H. Ikeno, H. Niwa, H. Kiuchi and Y. Harada, *Phys. Rev. B*, 2017, **96**, 214420.

14 D. Asakura, Y. Nanba, M. Okubo, H. Niwa, H. Kiuchi, J. Miyawaki, M. Oshima, E. Hosono and Y. Harada, *Phys. Chem. Chem. Phys.*, 2019, **21**, 26351–26357.

15 H. Wadati, D. Kobayashi, H. Kumigashira, K. Okazaki, T. Mizokawa, A. Fujimori, K. Horiba, M. Oshima, N. Hamada, M. Lippmaa, M. Kawasaki and H. Koinuma, *Phys. Rev. B: Condens. Matter Mater. Phys.*, 2005, **71**, 035108.

16 K. Momma and F. Izumi, *J. Appl. Crystallogr.*, 2011, **44**, 1272–1276.

17 D. Kumari, D. N. Singh, Md. K. Shamin, S. Chowdhury, R. J. Choudhary and S. Sharma, *J. Alloy. Compd.*, 2023, **967**, 171768.

18 E. Folven, Y. Takamura and J. K. Grepstad, *J. Electron Spectrosc. Relat. Phenom.*, 2012, **185**, 381–388.

19 T. Tsuyama, T. Matsuda, S. Chakraverty, J. Okamoto, E. Ikenaga, A. Tanaka, T. Mizokawa, H. Y. Hwang, Y. Tokura and H. Wadati, *Phys. Rev. B: Condens. Matter Mater. Phys.*, 2015, **91**, 115101.

20 I. Yamada, A. Tanaka, S. Oda, Y. Okazaki, F. Toda, Y. Kato, Y. Kizawa, M. Oshita, M. Goto, A. Morimura, A. Ochi, K. Toda, W. Wang, H. Yamamoto, H. Ikeno and S. Yagi, *Mater. Trans.*, 2023, **64**, 2097–2104.

21 P. C. Rogge, R. U. Chandrasena, A. Cammarata, R. J. Green, P. Shafer, B. M. Lefler, A. Huon, A. Arab, E. Arenholz, H. N. Lee, T.-L. Lee, S. Nemsák, J. M. Rondinelli, A. X. Gray and S. J. May, *Phys. Rev. Mater.*, 2018, **2**, 015002.

22 H. J. Lee, G. Kim, J.-S. Kang, B. Dabrowski, S. W. Han, S. S. Lee, C. Hwang, M. C. Jung, H. J. Shin, H. G. Lee, J.-Y. Kim and B. I. Min, *J. Appl. Phys.*, 2007, **101**, 09G523.

23 S. Eisebitt, T. Böske, J.-E. Rubensson and W. Eberhardt, *Phys. Rev. B: Condens. Matter Mater. Phys.*, 1993, **47**, 14103–14109.

24 A. J. Achkar, T. Z. Regier, E. J. Monkman, K. M. Shen and D. G. Hawthorn, *Sci. Rep.*, 2011, **1**, 182.

25 H. Wadati, A. J. Achkar, D. G. Hawthorn, T. Z. Regier, M. P. Singh, K. D. Truong, P. Fournier, G. Chen, T. Mizokawa and G. A. Sawatzky, *Appl. Phys. Lett.*, 2012, **100**, 193906.

26 D. Asakura, E. Hosono, Y. Nanba, H. Zhou, J. Okabayashi, C. Ban, P.-A. Glans, J. Guo, T. Mizokawa, G. Chen, A. J. Achkar, D. G. Hawthron, T. Z. Regier and H. Wadati, *AIP Adv.*, 2016, **6**, 035105.

27 A. J. Achkar, T. Z. Regier, H. Wadati, Y.-J. Kim, H. Zhang and D. G. Hawthorn, *Phys. Rev. B: Condens. Matter Mater. Phys.*, 2011, **83**, 081106.

28 M. Abbate, J. C. Fuggle, A. Fujimori, L. H. Tjeng, C. T. Chen, R. Potze, G. A. Sawatzky, H. Eisaki and S. Uchida, *Phys. Rev. B: Condens. Matter Mater. Phys.*, 1993, **47**, 16124–16130.

29 M. W. Haverkort, Z. Hu, J. C. Cezar, T. Burnus, H. Hartmann, M. Reuther, C. Zobel, T. Lorenz, A. Tanaka, N. B. Brookes, H. H. Hsieh, H.-J. Lin, C. T. Chen and L. H. Tjeng, *Phys. Rev. Lett.*, 2006, **97**, 176405.

30 M. Merz, P. Nagel, C. Pinta, A. Samartsev, H. V. Löhneysen, M. Wissinger, S. Uebe, A. Assmann, D. Fuchs and S. Schuppler, *Phys. Rev. B: Condens. Matter Mater. Phys.*, 2010, **82**, 174416.

31 Y. Yokoyama, Y. Yamasaki, M. Taguchi, Y. Hirata, K. Takubo, J. Miyawaki, Y. Harada, D. Asakura, J. Fujioka, M. Nakamura, H. Daimon, M. Kawasaki, Y. Tokura and H. Wadati, *Phys. Rev. Lett.*, 2018, **120**, 206402.

32 T. Mizokawa, Y. Wakisaka, T. Sudayama, C. Iwai, K. Miyoshi, J. Takeuchi, H. Wadati, D. G. Hawthorn, T. Z. Regier and G. A. Sawatzky, *Phys. Rev. Lett.*, 2013, **111**, 056404.

33 W. Zhang, E. Hosono, D. Asakura, H. Yuzawa, T. Ohigashi, M. Kobayashi, H. Kiuchi and Y. Harada, *Sci. Rep.*, 2023, **123**, 4639.

34 D. Asakura, T. Sudayama, Y. Nanba, E. Hosono, H. Kiuchi, K. Yamazoe, J. Miyawaki, Y. Harada, A. Yamada, R.-P. Wang and F. M. F. de Groot, *Phys. Chem. Chem. Phys.*, 2025, **27**, 4092–4098.

35 J. van Elp, J. L. Wieland, H. Eskes, P. Kuiper, G. A. Sawatzky, F. M. F. de Groot and T. S. Turner, *Phys. Rev. B: Condens. Matter Mater. Phys.*, 1991, **44**, 6090–6103.

36 E. Lee, D. H. Kim, J. Hwang, J.-S. Kang, N. Van Minh, I.-S. Yang, T. Ueno and M. Sawada, *J. Korean Phys. Soc.*, 2013, **62**, 1910–1913.

37 R. D. Shannon, *Acta Crystallogr. Sect. A*, 1976, **32**, 751–767.

38 M. Abbate, R. Potze, G. A. Sawatzky and A. Fujimori, *Phys. Rev. B: Condens. Matter Mater. Phys.*, 1994, **49**, 7210–7218.

39 F. Frati, M. O. J. Y. Hunault and F. M. F. de Groot, *Chem. Rev.*, 2020, **120**, 4056–4110.
40 S. Soni, M. Dave, B. Dalela, P. A. Alvi, S. Kumar, S. S. Sharma, D. M. Phase, M. Gupta and S. Dalela, *Appl. Phys. A*, 2020, **126**, 585.
41 T.-J. Ju, C.-H. Wang and S. D. Lin, *Catal. Sci. Technol.*, 2019, **9**, 2118–2124.
42 M. Varshney, A. Sharma, D. Prakash and K. D. Verma, *J. Phys. Chem. Solids*, 2024, **184**, 111721.
43 S. G. Minasian, E. R. Batista, C. H. Booth, D. L. Clark, J. M. Keith, S. A. Kozimor, W. W. Lukens, R. L. Martin, D. K. Shuh, S. C. E. Stieber, T. Tylisczcak and X. Wen, *J. Am. Chem. Soc.*, 2017, **139**, 18052–18064.
44 A. Yoko, Y. Omura, K. Ninomiya, M. Nishibori, T. Fujita, H. Kasai, E. Nishibori, N. Chiba, G. Seong, T. Tomai and T. Adschiri, *J. Am. Chem. Soc.*, 2024, **146**, 16324–16331.
45 E. Armenta-Jaime, J. Molina-González, K. P. Salas-Martin, R. Fan, L.-Y. Chang, J.-L. Chen, P. Steadman, H. Desirena-Enrriquez, A. Dutt, P. Olalde-Velasco and S. E. Castillo-Blum, *Phys. Chem. Chem. Phys.*, 2023, **25**, 20308–20319.
46 T. Nakamura, R. Oike, Y. Ling, Y. Tamenori and K. Amezawa, *Phys. Chem. Chem. Phys.*, 2016, **18**, 1564–1569.